Spatial coexistence of multiple modes in a nanogap spin Hall nano-oscillator with extended Pt/Ni/Fe trilayers

Lina Chen,[1,2] Wenqiang Wang,[2] Xiang Zhan,[2] Kaiyuan Zhou,[2] Zhenyu Gao,[2] Like Liang,[2] Tiejun Zhou,[3,*] Youwei Du,[2] and Ronghua Liu[2,†]

[1]*School of Science, Nanjing University of Posts and Telecommunications, Nanjing 210023, China*

[2]*Jiangsu Provincial Key Laboratory for Nanotechnology, School of Physics and National Laboratory of Solid State Microstructures, Nanjing University, Nanjing 210093, China*

[3]*Centre for Integrated Spintronic Devices, School of Electronics and Information, Hangzhou Dianzi University, Hangzhou 310018, China*

(Received 23 November 2021; revised 13 February 2022; accepted 1 March 2022; published 14 March 2022)

We experimentally study the microwave generation characteristics of a spin Hall nano-oscillator driven by a local spin current injected into a nanoscale region of extended Pt/Ni/Fe trilayers due to the spin Hall effect in the Pt layer and the interfacial Rashba effect at the Pt/Ni interface. The dependence of the generated microwave spectra on the exciting current and on the magnitude and angle of the magnetic field indicates that multiple spin-wave modes with either higher frequencies than the ferromagnetic resonance frequency f_{FMR} at low out-of-plane tilting angles and small fields or lower frequencies than f_{FMR} at high tilting angles and large fields are excited by local spin currents. Furthermore, the temperature dependence of the generated spectra in the extended Pt/Ni/Fe trilayers demonstrates that the thermally activated mode transition between these distinct dynamical modes is significantly suppressed. These results suggest that the observed multiple modes are physically separated in different local potential wells created by the spatial inhomogeneity of the internal field in the asymmetric ferromagnetic bilayer with strong interfacial exchange coupling and anisotropy fields. Finally, the very weak dependence of the minimum linewidth on temperature further confirms the lack of thermal-fluctuation-induced mode coupling and mode transition between these individual dynamical modes.

DOI: 10.1103/PhysRevB.105.104413

I. INTRODUCTION

Spin-orbit coupling (SOC) is a relativistic interaction between spin and orbital momentum that induces a variety of important effects and phenomena in spintronic devices [1]. For instance, the spin Hall effect (SHE) [2] and interfacial Rashba-Edelstein effect (IREE) enable the conversion between charge and spin currents and allow for the transfer of angular momentum between local magnetization and electrons' spin due to spin-transfer torque and exchange interaction [3,4]; the anomalous Hall effect [5], anisotropic magnetoresistance (AMR) [6], and the spin Seebeck effect [7] couple charge transport or thermal transport with magnetization orientation; and magnetocrystalline anisotropy [8] and the Dzyaloshinskii-Moriya interaction (DMI) [9,10] result in various nontrivial topological electronic structures and spin textures. Most of these effects already facilitate technological applications in various promising energy-efficient spin-based devices [11,12].

In spintronic devices based on multilayer structures, interfacial SOC as well as bulk SOC plays a crucial role in the generation of spin-orbit torques and emergence of nontrivial spin textures [3,4,13]. In particular, in the extensively studied heavy metal (HM)/ferromagnet (FM) bilayer systems, HMs with strong SOC generate spin currents that flow orthogonally to the in-plane currents due to the SHE and electrically control the reversal and coherent oscillation of magnetization of the adjacent FMs [1]. Meanwhile, in a HM/FM bilayer with broken inversion symmetry, the in-plane charge current also can generate a net spin polarization at the interface due to the IREE and exert a spin torque on adjacent magnetization via exchange interaction [4]. In addition, spin memory loss and magnon-scattering-induced additional damping are significantly related to the interface, including interfacial SOC, magnetic proximity, and interface defect and/or inhomogeneity [14,15]. On the other hand, the magnetic properties [e.g., magnetic anisotropy (MA), chiral DMI, interlayer exchange interaction, and inhomogeneous nature] of a thin multilayer highly depend on the interface between different HMs and magnetic materials [3]. Current-induced spin-current-driven magnetization oscillation, referred to as a spin Hall nano-oscillator (SHNO) [16,17], based on various HM/FM bilayers with abundant nonlinear spin-wave dynamics, e.g., self-localized bullet [16–23], propagating [24,25], and localized bubble skyrmion and droplet modes [24,26], has been demonstrated by experiments and simulations [27,28]. However, the FM1/FM2 ferromagnetic bilayer, with richer interfacial magnetic properties than a single FM layer, as the free FM layer of SHNOs still remains to be explored. Compared with the HM/FM bilayer system, the HM/FM1/FM2 trilayer system exhibits richer and more complex magnetic properties because it involves asymmetric magnetic layers,

*tjzhou@hdu.edu.cn
†rhliu@nju.edu.cn

interlayer exchange interaction, and additional interfacial MA and DMI at the FM1/FM2 interface besides those of the HM/FM interface. For example, a larger interfacial-DMI-induced chiral magnetic domain wall [29–31], spin-wave nonreciprocity [32], and spin reorientation transitions [33–35] have been found in Cu/Ni/Fe, W/Ni/Fe, and Pt/Co/Ni, respectively. The acoustic and optical ferromagnetic resonance (FMR) modes have been extensively studied by FMR experiments and theoretical models in various FM1/FM2 bilayer film systems [36,37]. Therefore, compared with the out-of-plane and in-plane magnetization Pt/FM-bilayer-based SHNOs, the Pt/Ni/Fe-trilayer-based SHNOs possess additional interfacial DMI and interlayer exchange coupling between the Fe and Ni layers, as well as an inhomogeneous and asymmetric magnetization nature, that could facilitate achieving some unique current-driven spin-wave dynamics.

Based on previous studies of the spin reorientation transitions in the HM/Ni/Fe trilayer [33–36], we adopt the Ni(2.5 nm)/Fe(0.9 nm) bilayer as the ferromagnetic layer of SHNOs to experimentally study the dependence of the microwave generation spectral characteristics on the excitation current, magnitude and angle of applied magnetic field, and temperature. In contrast to the Pt/Py-based SHNOs with a primary self-localized bullet mode at low currents accompanied by a secondary side mode at high currents [38], Pt/Ni/Fe-based SHNOs exhibit the coexistence of multiple dynamical modes with frequencies higher than or close to f_{FMR} for low polar angles $0 \leqslant \varphi \leqslant 60^{\circ}$ and below f_{FMR} for $\varphi > 60^{\circ}$ and large field $H > 1.5$ kOe. The absence of a noticeable dependence of the minimum linewidth on temperature suggests that the thermally activated mode transition between these dynamical modes is significantly suppressed by a high barrier potential between physically separated oscillation regions at cryogenic temperature, which is created by the spatial inhomogeneity of the internal field due to competition among demagnetization, interlayer exchange, and anisotropy energies.

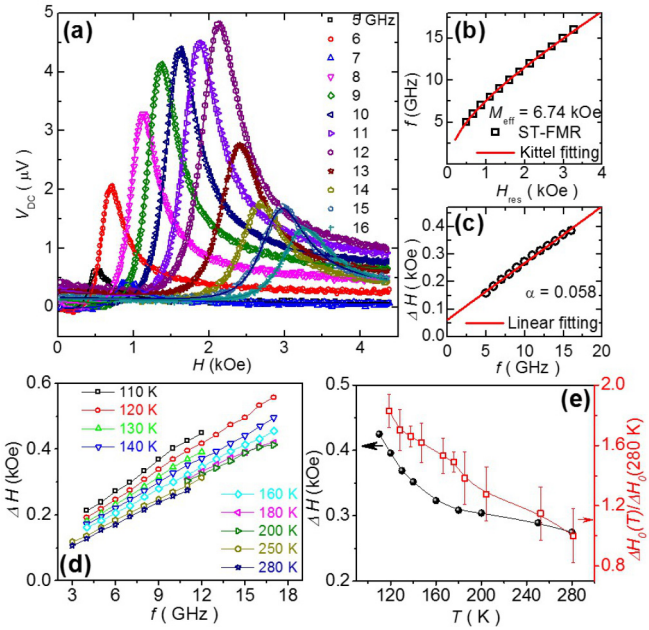

FIG. 1. ST-FMR spectra of the Pt(4 nm)/Ni(2.5 nm)/Fe(0.9 nm) trilayer under an in-plane magnetic field. (a) Symbols: the ST-FMR voltage V_{DC} vs in-plane magnetic field H obtained with various excitation frequencies from 5 to 16 GHz with a 1-GHz step at an angle $\theta = 60^{\circ}$ between the in-plane field H and the direction of current I and room temperature. The curve is the best fit with a sum of a symmetric and an antisymmetric Lorentzian function. (b) and (c) Dependence of the resonance field H_{res} (b) and the linewidth (c) on the excitation frequency f. The solid curve in (b) is the fitting result of the FMR data using the Kittel formula with a parameter $M_{\mathrm{eff}} = 6.74$ kOe. The solid line in (c) is a linear fitting of frequency-dependent linewidth ΔH data using $\Delta H = \Delta H_0 + \alpha f/\gamma$ with $\alpha = 0.058$ and $\Delta H_0 = 63$ Oe. (d) The linewidth ΔH vs f at labeled temperatures. (e) The ΔH obtained at $f = 11$ GHz (left vertical axis) and normalized $\Delta H_0(T)/\Delta H_0(280\ \mathrm{K})$ (right vertical axis) as a function of temperature.

II. EXPERIMENT

The test SHNO device structure and the experimental setup are the same as those used with our previously reported in-plane nanogap SHNOs [17]. The test device consists of a Pt(4 nm)/Ni(2.5 nm)/Fe(0.9 nm) multilayer disk with 4 μm diameter deposited on an annealed sapphire substrate by DC magnetron sputtering under ~3.7 mTorr Ar pressure. On the top, two pointed Au(80 nm) electrodes with ~100 nm gap on the Pt/Ni/Fe multilayer disk achieve a highly localized current density in the trilayer within the gap area. The device is fabricated by a combination of magnetron sputtering and electron beam lithography. Since the SHE-generated spin currents have in-plane spin polarization perpendicular to the direction of the applied charge current I, the magnetization **M** of the adjacent Ni/Fe layer will receive the maximum spin torque from the pure spin currents generated by the bottom Pt layer when it is also perpendicular to the direction of the current. The microwave-frequency voltage of the SHNO is generated by the current flowing through the magnetic layer due to its resistance oscillations associated with the anisotropic magnetoresistance (AMR) effect. The AMR shows the sinusoidal dependence of resistance on the orientation of **M** with a period of 180° between **M** and the current direction. Therefore, to trade off a reduction in the efficiency of the spin torque (ST) for a sizable generation microwave voltage for auto-oscillation spectra and rectification voltage for ST-FMR spectra arising from AMR, we chose the geometry of the in-plane component of the applied magnetic field forming an angle $\theta = 60^{\circ}$ with respect to the current direction for all spectroscopic measurements described below (as defined in the inset of Fig. 2).

III. RESULTS AND DISCUSSION

A. ST-FMR spectra

Based on previous reports [29–36], the Ni(2.5)/Fe(0.9) thin bilayer exhibits significant different magnetic properties from the soft magnetic Py [17] and [Co/Ni]n multilayer with strong perpendicular magnetic anisotropy (PMA) [24], and may have a strong influence on its spin-torque-driven dynamics. Therefore we first use a standard spin-torque–ferromagnetic-resonance (ST-FMR) technique to

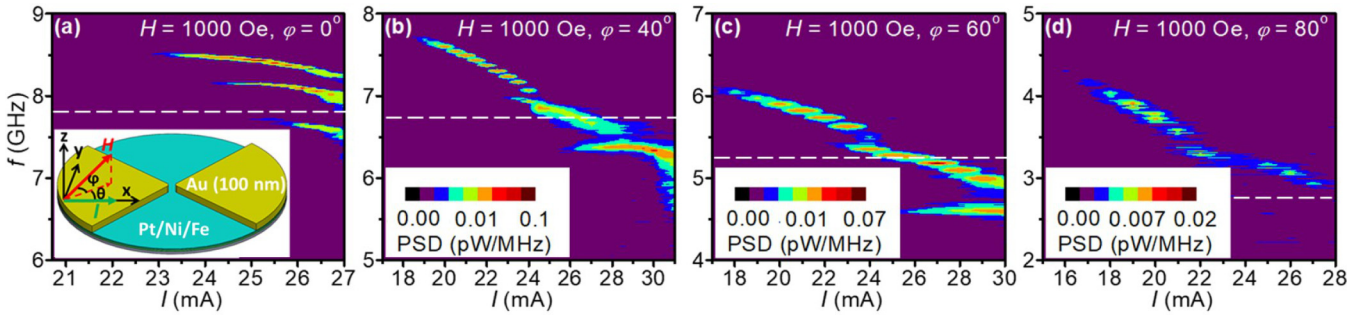

FIG. 2. Pseudocolor maps of the dependence of the generated microwave spectra on the current at $T = 6$ K, at applied magnetic field $H =$ 1000 Oe with four different out-of-plane tilting angles $\varphi = 0^\circ$ (a), 40° (b), 60° (c), and 80° (d). The dashed lines represent the corresponding FMR frequencies f_{FMR} of the trilayer thin film.

determine the FMR frequency f_{FMR} of the microsized Pt(4)/Ni(2.5)/Fe(0.9) thin film at various tilting angles of the external magnetic field. The ST-FMR spectra were recorded by scanning the applied magnetic field under the different excitation frequencies f from 5 to 16 GHz and $\theta = 60^\circ$. Figure 1(a) shows a representative ST-FMR voltage V_{DC} with in-plane field geometry, which can be well fitted by a sum of a symmetric and an antisymmetric Lorentzian function, consistent with previous studies [39]. The extracted resonance field H_{res} vs f agrees well with Kittel's formula $f = \gamma\sqrt{H(H + 4\pi M_{\mathrm{eff}})}$ [solid curve in Fig. 1(b)], from which the effective demagnetizing field $4\pi M_{\mathrm{eff}}$ can be determined to be 6.74 kOe. The interfaces of Pt/Ni and Ni/Fe can cause perpendicular magnetic anisotropy (PMA), which contributes the effective demagnetizing field in the form $4\pi M_{\mathrm{eff}} = 4\pi M_s - \frac{2K_u}{tM_s}$, where M_s is the saturation magnetization, K_u is the anisotropy coefficient, and $t = 3.4$ nm is the thickness of the Ni/Fe film. K_u was estimated to be 0.36 erg/cm^2 using M_s = 760 emu/cm^3 of the film measured by a vibration sample magnetometer at room temperature. The Gilbert damping α and inhomogeneous linewidth broadening ΔH_0 of the Ni/Fe film are also estimated by fitting the frequency-dependent resonance linewidth using the equation $\Delta H = \Delta H_0 + \alpha f/\gamma$, where γ is the gyromagnetic ratio. The damping constant α = 0.058 is two times larger than the value of 0.028 observed in Pt(5 nm)/Py(4 nm) [40], which is related to the additional magnon scattering at the Pt/Ni and Ni/Fe interfaces due to the interfacial SOC [41] and larger magnetoelastic efficiency in Ni, except for the expected spin-pumping effect in Pt/Ni due to spin current generation. In addition, the inhomogeneous linewidth broadening ΔH_0 reaches as much as 63 Oe, indicating that the studied Pt/Ni/Fe thin film has a significantly inhomogeneous nature due to the asymmetric magnetic layer, interlayer exchange interaction, and interfacial MA and DMI. To further characterize the temperature effect on the magnetic dynamics, we perform measurements of the isothermal ST-FMR spectra for temperatures in the range of 110–280 K. The FMR frequency f_{FMR} (with fixed external magnetic fields) has a slight increase with decreasing temperature at our studied temperature range due to the slow increase in the saturation magnetization M_s of the Ni/Fe bilayer. For instance, f_{FMR} at 1.5 kOe shows only an approximately 7% increase when the device cools down to 110 K from 280 K. In contrast to f_{FMR}, the linewidth ΔH and the inhomogeneous linewidth broadening ΔH_0 exhibit more significant broadening ($> 50\%$) with reducing temperature [Figs. 1(d) and 1(e)], suggesting that the spatial inhomogeneity of the magnetization properties, e.g., the interfacial MA and inhomogeneous nature (defect and/or grain-boundary-induced pinning effect), significantly increases with reducing temperature due to the suppression of thermal fluctuation at cryogenic temperatures. Additionally, we can quantitatively estimate an effective spin-orbit-torque (SOT) efficiency $\zeta_{\mathrm{ST}} = 0.07$ of this trilayer structure at room temperature by line-shape analysis of the ST-FMR spectra, which is noticeably higher than the previous reported values of $\sim$0.05 in Pt(7.4 nm)/Ni(4 nm) [42] and 0.056 ± 0.005 in Pt(6 nm)/Py(4 nm) [40]. The difference suggests that these Pt-based magnetic heterostructures exhibit different interfacial spin transparency due to interface-dependent spin backflow and spin memory loss, as well interfacial spin torques generated by IREE due to different interfaces and thicknesses [4,15,42,43].

B. Microwave generation spectra characteristics of dynamical modes at $T = 6$ and 100 K

To study ST-driven spin-wave dynamics of the Pt/Ni/Fe-trilayer-based SHNOs, we investigate the dependence of the spectral characteristics of a nanogap SHNO on the excitation current I at different out-of-plane tilting angles φ. Figure 2 shows a representative current dependence of the microwave power spectral density (PSD) of the test device at four selected polar angles φ. Differing from the previously reported single primary bullet mode in Pt/Py-based SHNOs and localized bullet and propagating modes in Pt/[Co/Ni]$_n$-based SHNOs, three main peaks are observed in the microwave generation spectra above the critical current I_c, substrate temperature T = 6 K, $\varphi = 0^\circ$–80°, and $H = 1000$ Oe [Figs. 2(a)–2(d)]. The oscillation mode with the highest frequency above the FMR frequency f_{FMR} (dashed lines) of the Pt/Ni/Fe trilayer film is firstly excited at low current and exhibits a significant redshift with increasing current. The middle frequency peak also shows a redshift with increasing current, but its frequency is close to f_{FMR}. The third peak with a frequency below f_{FMR} shows a significant redshift at large currents as well. These multiple dynamic behaviors are different from the observed single nonlinear self-localized bullet mode in in-plane nanogap SHNOs with a negligible MA Py/Pt bilayer extended film, but are reminiscent of the observed multiple modes transition and coexistence among propagating, dynamical bubble,

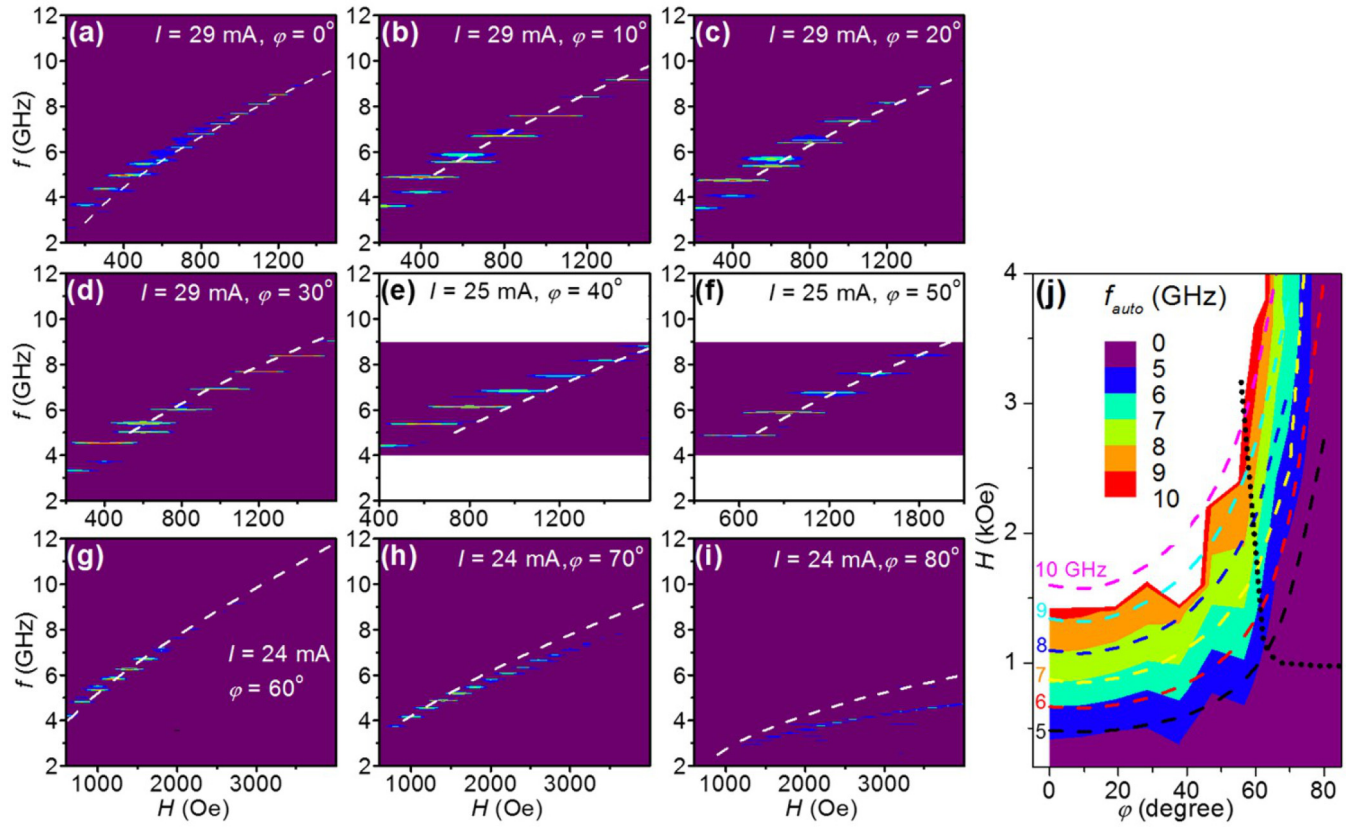

FIG. 3. Dependence of the microwave generation characteristics of the SHNO on the external magnetic field with various out-of-plane tilting angles. (a)–(i) Pseudocolor maps of the field-dependent spectra obtained at $T = 6$ K with labeled excited current, under different out-of-plane tilting angles $\varphi = 0^\circ$ (a), 10° (b), 20° (c), 30° (d), 40° (e), 50° (f), 60° (g), 70° (h), and 80° (i). The dashed curves represent f_{FMR} vs H dispersion curves of the Pt/Ni/Fe thin film obtained by the ST-FMR technique. (j) Contour plot in terms of frequency f_c of SHNO extracted from Lorentzian fitting of the spectra of (a)–(i) in the plane of the amplitude and the tilting angle φ of the external field. The dashed curves represent the dispersion relation between the external field and the FMR frequencies f_{FMR} at various angles φ. The dotted curve denotes the crossover boundary between the auto-oscillation frequency f_{auto} and f_{FMR}. f_{FMR} becomes higher than f_{auto} when φ crosses the dotted line from 0° to 80°.

and localized bullet modes at low in-plane fields ($\leqslant 500$ Oe) in SHNOs with a suitable PMA Pt/[Co/Ni]$_n$ film due to a bubble domain structure and/or various spatially inhomogeneous fields. In addition, the almost independent evolution of the intensity and frequency with the excitation current among the oscillation modes indicates that these oscillations are related to spatially different oscillation regions.

To explore the relationship between the observed dynamical modes and the external magnetic field, we investigate the dependence of the generation spectrum on the external fields H at different polar angles φ from 0° to 80° (Fig. 3). The dashed curves show the dispersion relation between the FMR frequency f_{FMR} and applied field determined by using the ST-FMR technique. One can see that the frequencies of dynamical modes are higher than or close to the uniform FMR frequency f_{FMR} at low tilting angles $\varphi \leqslant 60^\circ$ [lower left corner below the dotted curve in Fig. 3(j)], and then the oscillations transform into the low-frequency localized modes regime at high tilting angles $\varphi > 60^\circ$ and large fields [top right corner above the dotted curve in Fig. 3(j)]. This behavior is different from the previous nanocontact spin-transfer-torque nano-oscillator (STNO), which shows the dynamical mode transition from the nonlinear localized bullet mode at low tilting angles to the quasilinear propagating mode at high tilting angles due to change in the nonlinear coefficient sign of the STNO with magnetization orientation [44–46]. However, it is consistent with our previously studied Pt/[Co/Ni]-based SHNOs with a suitable PMA [25,26]. To better illustrate the dependence of microwave generation spectra on the magnitude and orientation of the field, we summarize the field dependence of the frequency characteristic of the SHNO and uniform f_{FMR} of the Pt/Ni/Fe thin film in the phase diagram [Fig. 3(j)], where the oscillation frequencies f_{auto} of SHNO are represented in the contour plot in the plane of the amplitude and the tilting angle φ of the external field. Additionally, we note that the multiple dynamic modes are also excited simultaneously at high currents for large tilting angles $\varphi > 50^\circ$, which can be clearly seen in the following results obtained at high temperatures.

C. Temperature effect of current-driven dynamical modes

To gain a more comprehensive understanding of the experimental parameter dependence and thermal effect on the characteristics of those localized modes, we further perform the spectroscopic measurements with varying current and

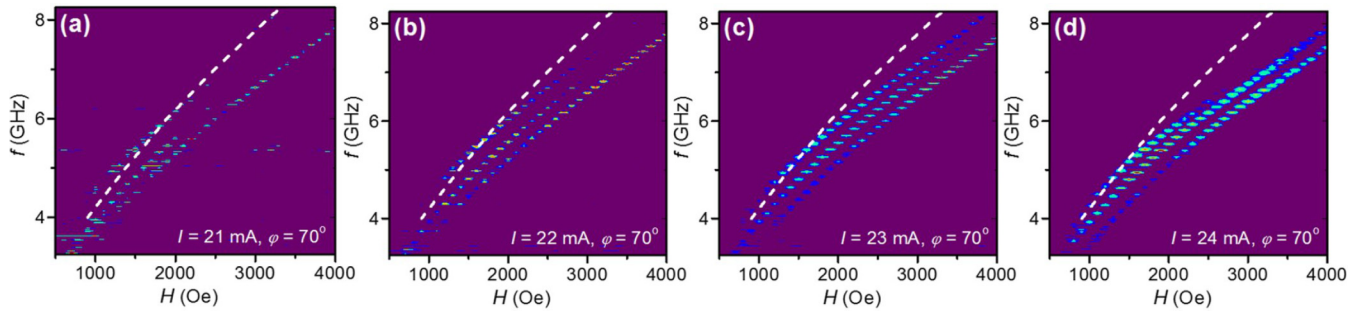

FIG. 4. Pseudocolor maps of the field-dependent spectra obtained at $T = 100$ K, the out-of-plane tilting angle $\varphi = 70^\circ$, and four selected excited currents $I = 21$ mA (a), 22 mA (b), 23 mA (c) and 24 mA (d). The dashed curves represent the f_{FMR} vs H dispersion curve of the Pt/Ni/Fe thin film obtained by the ST-FMR technique at the same φ.

fields at two representative $\varphi = 0^\circ$ and 70° orientations and cryogenic temperatures from 6 to 200 K. Figure 4 shows the substantial field-dependent spectra obtained at substrate temperature $T = 100$ K, $\varphi = 70^\circ$, and four selected excitation currents $I = 21$, 22, 23, and 24 mA. Similar to the spectra obtained at 6 K, three primary oscillating peaks are observed simultaneously in a wide range of fields (e.g., 1–4 kOe for $I = 23$ mA) and show distinct spectral characteristics without mode transition, hopping, and synchronization behaviors due to mode coupling. The highest-frequency mode has an oscillation frequency higher than f_{FMR} and a weak nonlinear redshift below field $H < 1.5$ kOe. However, for large fields, the oscillation frequencies of all three modes are below f_{FMR} and exhibit a significant redshift with increasing current.

The detailed dependence of the spectral characteristics on I at small in-plane fields and different temperatures is shown in Fig. 5. Like the representative spectra obtained at 6 K and 1000 Oe in Fig. 2(a) above, all current-dependent spectra obtained at different temperatures and external fields exhibit similar overall behavior as follows. First, one oscillation peak with frequency higher than f_{FMR} is observed above the critical current, and then it coexists with another one or two oscillation peaks with increasing excitation current. Second, the oscillation frequencies at their onset currents almost keep constant with increasing temperature, consistent with the previous Pt/Py- and Pt/$[\mathrm{Co/Ni}]_n$-based SHNOs. Third, these observed oscillation peaks show the independent evolution of the intensity and frequency with the excitation current and are not noticeably affected by the presence of

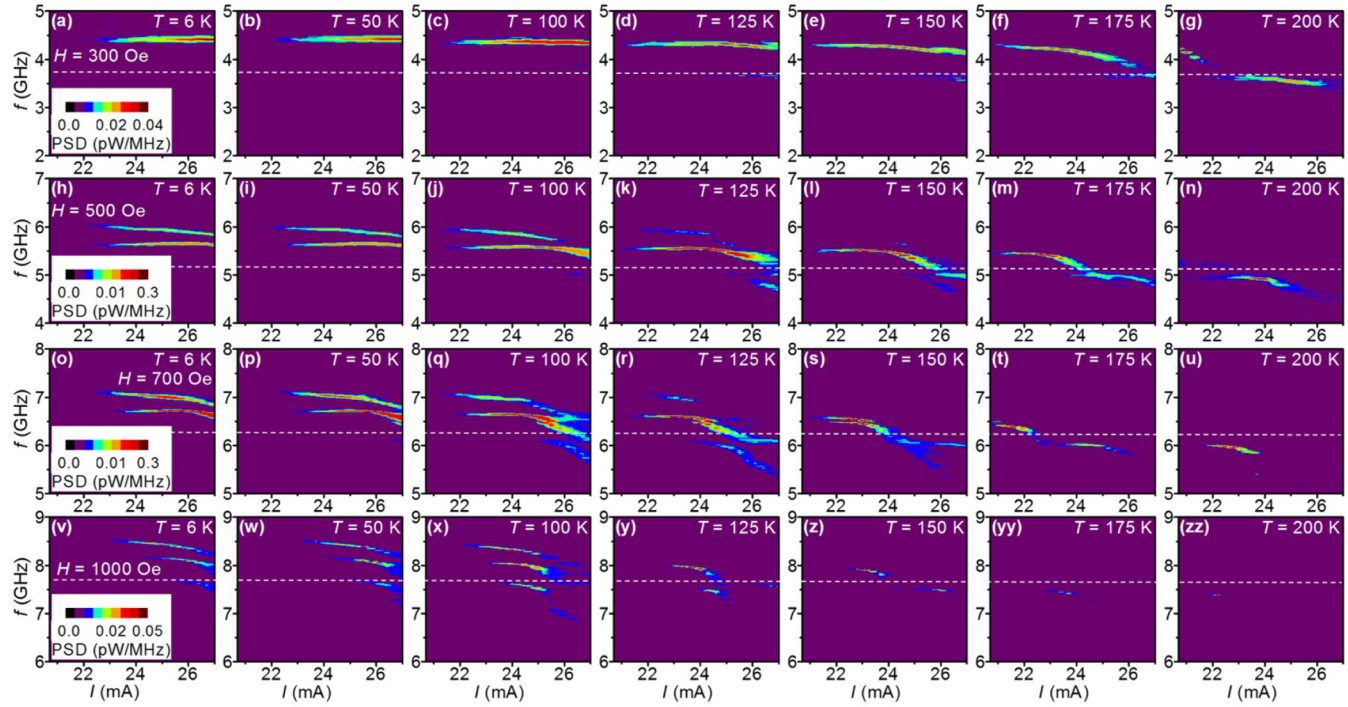

FIG. 5. Temperature dependence of the microwave generation characteristics of the SHNO at several selected in-plane magnetic fields $\varphi = 0$. (a)–(g) Pseudocolor maps of the current-dependent spectra obtained under $H = 300$ Oe, at $T = 6$ K (a), 50 K (b), 100 K (c), 125 K (d), 150 K (e), 175 K (f), and 200 K (g). (h)–(n) Same as (a)–(g), except $H = 500$ Oe. (o)–(u) Same as (a)–(g), except $H = 700$ Oe. (v)–(z), (yy), and (zz) Same as (a)–(g), except $H = 1000$ Oe. The dashed lines are the f_{FMR} obtained by the ST-FMR technique.

other modes, indicating that they are physically localized in different spatial regions without the visible mode hopping and transition behaviors caused by direct or indirect mode coupling. In previous studies, the main coupling between modes can be caused by thermal-magnon-mediated scattering coupling arising from the interaction between the dominant modes and the bath of thermally excited magnons, and the thermal-magnon population is affected not only by experimental temperature but also by the applied current because of the current-driven spin current, spin pumping, and current-induced Joule heating of the active device area. The lack of mode-coupling-induced mode hopping and thermal-activated mode transition indicates that there exists a considerable energy barrier between these separate spatial oscillation regions to suppress thermal-magnon-mediated scattering coupling due to the spatial inhomogeneity of the magnetic properties of the Ni/Fe bilayer system at cryogenic temperature. These behaviors are distinct from those of SHNOs with an external Pt/Py bilayer [17]. The reason is likely related to the distinct magnetic properties between Py and Ni/Fe thin films. For instance, the soft ferromagnetic permalloy thin film has a negligible magnetic anisotropy and near-zero magnetoelastic coefficient. In contrast, the thin Ni/Fe bilayer exhibits a substantial magnetic anisotropy, interfacial DMI and interlayer exchange interaction, large magnetoelastic coefficient, and thickness-dependent spin-reorientation phenomenon [29–37].

To determine whether the behaviors discussed above are the general features of Pt/Ni/Fe-based SHNO, we also performed the measurement of current-dependent spectral characteristics at the tilting angle $\varphi = 70^\circ$, selected large fields, and selected temperatures, as shown in Fig. 6. Similar to what was observed at in-plane fields (Fig. 5), the microwave generation characteristics at $\varphi = 70^\circ$ show the multimodal coexistence behavior for all test temperatures and external fields, which further confirms the reason for the multimodal dynamics discussed above.

To gain further insight into the thermal effects on the multimodal dynamics of SHNO, we quantitatively analyze the generation linewidth of one oscillation mode as a function of temperature. To take into account Joule heating, we numerically evaluated the temperature increase in the active region of the device using COMSOL simulations with the previously reported resistivity and thermal conductivity of Pt/Ni/Fe thin films, Au, sapphire substrate, and the interface thermal resistance between the metal film and sapphire substrate [47–51]. Consistent with our previous Pt/Py bilayer system [38], the increased temperature of the Ni/Fe bilayer is localized in the center region of the device with a dumbbell shape transverse to the current flow and a maximum at the center of the nanogap [see Fig. 7(a)]. At a representative driving current of 26 mA and substrate temperature T of 50 K, the central temperature T_a reaches a maximum of ~178 K [Fig. 7(a)]. Figure 7(b) shows the minimum linewidth of the primary mode vs actual temperature T_a, which are extracted by Lorentzian fitting of the spectra obtained at three selected in-plane fields, 0.3, 0.5, and 0.7 kOe (Fig. 5). In contrast to the exponential increase in the linewidth due to the thermal-activated mode transition observed in Pt/Py-based SHNOs [17] and the observed significant broadening of the linewidth due to mode hopping in STNOs [52,53], the minimum linewidth does not exhibit a noticeable dependence on temperature. The other two secondary peaks exhibit a similar temperature dependence of the linewidth. This also further confirms that mode-coupling-caused mode hopping and mode transition, which significantly affect the dynamical

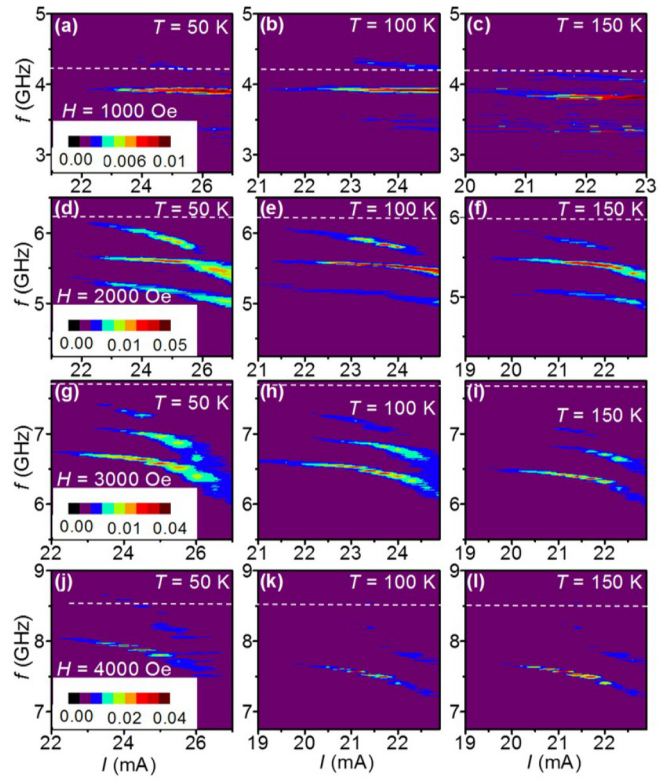

FIG. 6. Temperature dependence of the microwave generation characteristics of the SHNO at several selected magnetic fields with a large out-of-plane tilting angle $\varphi = 70^\circ$. (a)–(g) Pseudocolor maps of the current-dependent spectra obtained at oblique field $\varphi = 70^\circ$, $H = 1000$ Oe, and $T = 50$ K (a), 100 K (b), and 150 K (c). (d)–(f) Same as (a)–(c), except $H = 2000$ Oe. (g)–(i) Same as (a)–(c), except $H = 3000$ Oe. (j)–(l) Same as (a)–(c), except $H = 4000$ Oe. f_{FMR} are marked as the dashed lines.

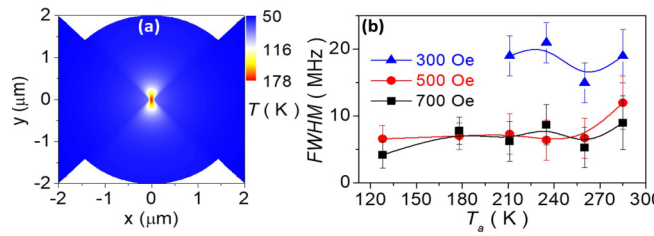

FIG. 7. (a) The representative calculated spatial map of temperature in the Ni/Fe bilayer at $I = 26$ mA and substrate temperature $T = 50$ K. (b) Actual temperature T_a of the center region of the device vs the full width at half maximum (FWHM) of the generated microwave spectra obtained at three in-plane magnetic fields. The symbols are the minimum linewidth corresponding to the highest peak PSD of the primary mode, which is extracted from Lorentzian fitting of the PSD spectra in Figs. 5(a)–5(u). The solid curves are given as guides to the eye.

coherence, are avoided by suppressing the thermal fluctuation at cryogenic temperatures and by the presence of a high local energy barrier between different oscillation regions due to the spatial inhomogeneity of the magnetic properties. The large remanent linewidth at low temperature for the low fields indicates that spin-current-driven dynamical coherence in the studied Pt/Ni/Fe-based SHNO is dominated by the spatial inhomogeneity, rather than the thermal broadening that causes a linear increase with temperature due to thermal fluctuation.

IV. CONCLUSION

To summarize, we find that in-plane nanogap SHNOs based on the extended magnetic Pt/Ni/Fe trilayer with asymmetric and inhomogeneous magnetization nature generally exhibit the coexistence of multiple dynamical modes with distinct oscillation frequencies at certain currents and fields. At small fields and low tilting angles, spectra characteristics, including current-induced frequency redshift and oscillation frequency higher than or close to f_{FMR} of the thin film, suggest that these modes are related to propagating and field-localized modes due to a spatially inhomogeneous internal field including a domain-induced dipolar field, interfacial DMI, MA, and exchange fields. At large fields $H > 1.5$ kOe and high tilting angles $\varphi \geqslant 70^{\circ}$, the oscillation frequencies of all observed modes were below f_{FMR}, suggesting that all these modes belong to localized spin-wave modes. Furthermore, the temperature dependence of the spectra confirms the absence of mode transition and mode hopping, suggesting that these individual oscillation modes are physically localized in different regions due to the strong spatial inhomogeneity of the magnetic properties because the Pt/Ni/Fe trilayer exhibits an asymmetric and highly inhomogeneous magnetization nature. The high energy barrier between these physically separated oscillation regions prevents mode-coupling-induced mode hopping and thermal-activated mode transition, which in turn can prevent the exponential broadening of linewidth with increasing temperature and ensure the coherence of the generated microwave signals under considerable thermal fluctuation. Our results suggest that the intrinsic spatial deviation of magnetization of special films, as well as the previously reported local dipole field from the edge of nanoconstriction [19,20,54] or the additional magnetic nanoparticle [55,56], can be used to facilitate and restrict current-induced spin-wave dynamics in the external magnetic film.

ACKNOWLEDGMENTS

We acknowledge support from the National Natural Science Foundation of China (Grants No. 11774150, No. 12074178, No. 12004171, and No. 11874135), the Applied Basic Research Programs of Science and Technology Commission Foundation of Jiangsu Provinced (Grant No. BK20200309), the Open Research Fund of Jiangsu Provincial Key Laboratory for Nanotechnology, the Scientific Foundation of Nanjing University of Posts and Telecommunications (NUPTSF) (Grant No. NY220164), and Key Research and Development Program of Zhejiang Province (Grant No. 2021C01039).

[1] A. Manchon, J. Zelezny, I. M. Miron, T. Jungwirth, J. Sinova, A. Thiaville, K. Garello, and P. Gambardella, Rev. Mod. Phys. **91**, 035004 (2019).
[2] J. Sinova, S. O. Valenzuela, J. Wunderlich, C. H. Back, and T. Jungwirth, Rev. Mod. Phys. **87**, 1213 (2015).
[3] F. Hellman, A. Hoffmann, Y. Tserkovnyak, G. S. D. Beach, E. E. Fullerton, C. Leighton, A. H. MacDonald, D. C. Ralph, D. A. Arena, H. A. Dürr, P. Fischer, J. Grollier, J. P. Heremans, T. Jungwirth, A. V. Kimel, B. Koopmans, I. N. Krivorotov, S. J. May, A. K. Petford-Long, J. M. Rondinelli *et al.*, Rev. Mod. Phys. **89**, 025006 (2017).
[4] V. P. Amin, P. M. Haney, and M. D. Stiles, J. Appl. Phys. (Melville, NY) **128**, 151101 (2020).
[5] N. Nagaosa, J. Sinova, S. Onoda, A. H. MacDonald, and N. P. Ong, Rev. Mod. Phys. **82**, 1539 (2010).
[6] M. Trushin, K. Vyborny, P. Moraczewski, A. A. Kovalev, J. Schliemann, and T. Jungwirth, Phys. Rev. B **80**, 134405 (2009).
[7] G. E. W. Bauer, E. Saitoh, and B. J. van Wees, Nat. Mater. **11**, 391 (2012).
[8] S. S. A. Razee, J. B. Staunton, and F. J. Pinski, Phys. Rev. B **56**, 8082 (1997).
[9] I. Dzyaloshinsky, J. Phys. Chem. Solids **4**, 241 (1958).
[10] T. Moriya, Phys. Rev. **120**, 91 (1960).
[11] I. Zutic, J. Fabian, and S. Das Sarma, Rev. Mod. Phys. **76**, 323 (2004).
[12] Y. Cao, G. Xing, H. Lin, N. Zhang, H. Zheng, and K. Wang, iScience **23**, 101614 (2020).
[13] R. H. Liu, W. L. Lim, and S. Urazhdin, Phys. Rev. B **89**, 220409(R) (2014).
[14] L. J. Zhu, D. C. Ralph, and R. A. Buhrman, Phys. Rev. Lett. **122**, 077201 (2019).
[15] K. Gupta, R. J. H. Wesselink, R. X. Liu, Z. Yuan, and P. J. Kelly, Phys. Rev. Lett. **124**, 087702 (2020).
[16] V. E. Demidov, S. Urazhdin, H. Ulrichs, V. Tiberkevich, A. Slavin, D. Baither, G. Schmitz, and S. O. Demokritov, Nat. Mater. **11**, 1028 (2012).
[17] R. H. Liu, W. L. Lim, and S. Urazhdin, Phys. Rev. Lett. **110**, 147601 (2013).
[18] M. Ranjbar, P. Drrenfeld, M. Haidar, E. Iacocca, M. Balinskiy, T. Q. Le, M. Fazlali, A. Houshang, A. Awad, R. K. Dumas, and J. Åkerman, IEEE Magn. Lett. **5**, 3000504 (2014).
[19] V. E. Demidov, S. Urazhdin, A. Zholud, A. V. Sadovnikov, and S. O. Demokritov, Appl. Phys. Lett. **105**, 172410 (2014).
[20] Z. Duan, A. Smith, L. Yang, B. Youngblood, J. Lindner, V. E. Demidov, S. O. Demokritov, and I. N. Krivorotov, Nat. Commun. **5**, 5616 (2014).
[21] H. Mazraati, S. Chung, A. Houshang, M. Dvornik, L. Piazza, F. Qejvanaj, S. Jiang, T. Q. Le, J. Weissenrieder, and J. Åkerman, Appl. Phys. Lett. **109**, 242402 (2016).
[22] M. Collet, X. de Milly, O. d'Allivy Kelly, V. V. Naletov, R. Bernard, P. Bortolotti, J. Ben Youssef, V. E. Demidov, S. O.

Demokritov, J. L. Prieto, M. Munoz, V. Cros, A. Anane, G. de Loubens, and O. Klein, Nat. Commun. **7**, 10377 (2016).
[23] M. B. Jungfleisch, W. Zhang, J. Sklenar, J. Ding, W. Jiang, H. Chang, F. Y. Fradin, J. E. Pearson, J. B. Ketterson, V. Novosad, M. Wu, and A. Hoffmann, Phys. Rev. Lett. **116**, 057601 (2016).
[24] R. H. Liu, W. L. Lim, and S. Urazhdin, Phys. Rev. Lett. **114**, 137201 (2015).
[25] L. Chen, S. Urazhdin, Y. W. Du, and R. H. Liu, Phys. Rev. Appl. **11**, 064038 (2019).
[26] L. Chen, S. Urazhdin, K. Zhou, Y. W. Du, and R. H. Liu, Phys. Rev. Appl. **13**, 024034 (2020).
[27] V. E. Demidov, S. Urazhdin, G. de Loubens, O. Klein, V. Cros, A. Anane, and S. O. Demokritov, Phys. Rep. **673**, 1 (2017).
[28] L. Li, L. Chen, R. Liu, and Y. Du, Chin. Phys. B **29**, 117102 (2020).
[29] G. Chen, J. Zhu, A. Quesada, J. Li, A. T. N'Diaye, Y. Huo, T. P. Ma, Y. Chen, H. Y. Kwon, C. Won, Z. Q. Qiu, A. K. Schmid, and Y. Z. Wu, Phys. Rev. Lett. **110**, 177204 (2013).
[30] G. Chen, M. Robertson, H. Kwon, C. Won, A. K. Schmid, and K. Liu, J. Vac. Sci. Technol. A **39**, 053410 (2021).
[31] M. C. Robertson, C. J. Agostino, G. Chen, S. P. Kang, A. Mascaraque, E. GarciaMichel, C. Won, Y. Wu, A. K. Schmid, and K. Liu, Phys. Rev. B **102**, 024417 (2020).
[32] K. Di, V. L. Zhang, H. S. Lim, S. C. Ng, M. H. Kuok, J. Yu, J. Yoon, X. Qiu, and H. Yang, Phys. Rev. Lett. **114**, 047201 (2015).
[33] J.-S. Lee, J. T. Sadowski, H. Jang, J.-H. Park, J.-Y. Kim, J. Hu, R. Wu, and C.-C. Kao, Phys. Rev. B **83**, 144420 (2011).
[34] Y. Zhao, J. Ye, C. L. Gao, B. Ma, and Q. Y. Jin, J. Appl. Phys. (Melville, NY) **94**, 5100 (2003).
[35] J. Choi, J. Wu, C. Won, Y. Z. Wu, A. Scholl, A. Doran, T. Owens, and Z. Q. Qiu, Phys. Rev. Lett. **98**, 207205 (2007).
[36] B. Heinrich, S. T. Purcell, J. R. Dutcher, K. B. Urquhart, J. F. Cochran, and A. S. Arrott, Phys. Rev. B **38**, 12879 (1988).
[37] G. B. G. Stenning, L. R. Shelford, S. A. Cavill, F. Hoffmann, M. Haertinger, T. Hesjedal, G. Woltersdorf, G. J. Bowden, S. A. Gregory, and C. H. Back, New J. Phys. **17**, 013019 (2015).
[38] L. Chen, K. Zhou, S. Urazhdin, W. Jiang, Y. W. Du, and R. H. Liu, Phys. Rev. B **100**, 104436 (2019).
[39] L. Yang, Y. Fei, K. Zhou, L. Chen, Q. Fu, L. Li, C. Yan, H. Li, Y. W. Du, and R. H. Liu, Appl. Phys. Lett. **118**, 032405 (2021).
[40] L. Liu, T. Moriyama, D. C. Ralph, and R. A. Buhrman, Phys. Rev. Lett. **106**, 036601 (2011).
[41] L. Zhu, L. Zhu, D. C. Ralph, and R. A. Buhrman, Phys. Rev. Appl. **13**, 034038 (2020).
[42] H. Hayashi, A. Musha, H. Sakimura, and K. Ando, Phys. Rev. Research **3**, 013042 (2021).
[43] C.-F. Pai, Y. Ou, L. H. Vilela-Leao, D. C. Ralph, and R. A. Buhrman, Phys. Rev. B **92**, 064426 (2015).
[44] W. H. Rippard, M. R. Pufall, S. Kaka, T. J. Silva, and S. E. Russek, Phys. Rev. B **70**, 100406(R) (2004).
[45] A. Slavin and V. Tiberkevich, IEEE Trans. Magn. **44**, 1916 (2008); **45**, 1875 (2009).
[46] S. Bonetti, V. Tiberkevich, G. Consolo, G. Finocchio, P. Muduli, F. Mancoff, A. Slavin, and J. Åkerman, Phys. Rev. Lett. **105**, 217204 (2010).
[47] COMSOL MULTIPHYSICS, COMSOL AB, Stockholm, Sweden, https://www.comsol.com.
[48] E. T. Swartz and R. O. Pohl, Appl. Phys. Lett. **51**, 2200 (1987).
[49] H. K. Lyeo and D. G. Cahill, Phys. Rev. B **73**, 144301 (2006).
[50] R. J. Stoner and H. J. Maris, Phys. Rev. B **48**, 16373 (1993).
[51] X. Zhang, Q. G. Zhang, B. Y. Cao, M. Fujin, K. Takahashi, and T. Ikuta, Chin. Phys. Lett. **23**, 936 (2006).
[52] E. Iacocca, O. G. Heinonen, P. K. Muduli, and J. Åkerman, Phys. Rev. B **89**, 054402 (2014).
[53] O. G. Heinonen, P. K. Muduli, E. Iacocca, and J. Åkerman, IEEE Trans. Magn. **49**, 4398 (2013).
[54] A. Smith, K. Sobotkiewich, A. Khan, E. A. Montoya, L. Yang, Z. Duan, T. Schneider, K. Lenz, J. Lindner, K. An, X. Li, and I. N. Krivorotov, Phys. Rev. B **102**, 054422 (2020).
[55] C. Zhang, Y. Pu, S. A. Manuilov, S. P. White, M. R. Page, E. C. Blomberg, D. V. Pelekhov, and P. C. Hammel, Phys. Rev. Appl. **7**, 054019 (2017).
[56] C. Zhang, I. Lee, Y. Pu, S. A. Manuilov, D. V. Pelekhov, and P. C. Hammel, Nano Lett. **21**, 10208 (2021).